Article

Design and Optimization of an Inductively Coupled Power Transfer System for the Underwater Sensors of Ocean Buoys

Cheng Fang, Xingfei Li *, Ziming Xie, Jiayi Xu and Linling Xiao

State Key Laboratory of Precision Measuring Technology and Instruments, Tianjin University, Tianjin 300072, China; fangcheng@tju.edu.cn (C.F.); xzm1988@126.com (Z.X.); xjy0125@tju.edu.cn (J.X.); xiaolinling@tju.edu.cn (L.X.)

* Correspondence: lxftju@hotmail.com; Tel.: +86-22-2740-3707

Abstract: Batteries are commonly used as the power source of present underwater sensors of ocean buoys. However, batteries need to be frequently replaced, which is costly. To implement the real-time power supply for a buoy's underwater sensor, a new inductively coupled power transfer (ICPT) system that consists of two couplers and a closed cable is proposed in this paper. The special closed cable, which is the both mooring cable and transmission media, is designed to diminish the influence of changes on impedance. A model of the particular ICPT system is established. Optimization of system parameters are carried out based on the model and verified by means of the simulations. Resonant compensation is used to improve the power transfer performance. Finally, many experiments are implemented to compare with the original prototype. It is confirmed that this system can help solve the difficulty of the energy limit to a buoy's underwater sensor.

1. Introduction

Nowadays, ocean monitoring has attracted an increasing amount of attention, as it enables the prediction of global climate changes. Buoys, commonly used ocean monitor equipment, can be used to measure hydrological and weather information of a given position by sensors mounted on the buoy body and a mooring cable used to fix buoy's position. Plenty of buoys are able to establish an ocean monitoring network to implement area monitoring.

Ocean monitoring is a long-term process; therefore, it is critical that the ocean buoy has both a low cost of maintenance and a high reliability. At present, the battery which is chiefly used as the power source of the underwater sensors of existing buoys needs to be replaced frequently when it runs low on power, which is costly. Reducing the measuring frequency may allow for a long measurement period, but the monitoring capability is limited. Many scholars have been working on how to extend the battery life based on the point of energy efficiency, and many excellent achievements have been presented [1–3]. Nevertheless, these methods have not radically solved the problem of power limits. In theory, an electric cable can be used to transfer electric power from buoys to underwater sensors. However, this method is barely applied because it is not very reliable and unsuitable for multi-sensors. The capability of a real-time power supply for underwater sensors will dramatically enhance the monitoring performance of ocean buoys.

Due to the advantage of noncontact connection, an inductively coupled power transfer (ICPT) system has recently made great developments in special fields such as electric vehicles, mobile devices, and biomedical implants [4–9]. In the harsh underwater environment, ICPT technology is

preferable for its ease of use and reliability. Many recent studies of underwater ICPT systems have focused on the power supply for autonomous underwater vehicles [10–15]. This kind of ICPT system requires extra power source stations on the seafloor that are connected to electric substations via submarine cable. Since the power source is an electric substation, this system is suitable for high-power equipment. For the application of the ICPT system to ocean buoys, very few studies can be found. Paper [16] introduced a contactless underwater power transfer system, which may be utilized for ocean buoys. In this paper, the losses in cable are discussed, and a prototype inductive coupler is designed. Experimental results indicate that approximate 2 kW of power can be transferred to load without considering cable losses. The structure of the cable is not described in this paper, but it has great influence on compensation. Paper [17] proposed a power feeding system using magnetic coupling for an ocean observation mooring buoy. The primary coil is wound around the underwater wire, which is connected to the buoy, and the secondary coil, which is wound around a short segment of underwater wire, is parallel to the primary coil. On account of the fact that no ferromagnetic core exists, the system's leakage flux is high. Meanwhile, the installation of underwater coils and sensors is inconvenient. In the case of a 4.8 m mooring wire, the maximum power received by the sensor is merely 180 mW. Members of our team have published several papers on the circuit design of the ICPT system for ocean buoys, but the model and optimization of power transfer were not elaborated [18,19].

An ICPT system applied to transfer electric power to an underwater sensor of an ocean buoy in real time is detailed in this paper. To ensure the stability of power transfer, a special mooring cable is designed to decrease the influence of its changes in impedance. For the purpose of transmitting data in the same path (not introduced in this paper), two couplers are employed in this system. The model of this special ICPT system is established here. An analysis of parameters is discussed according to the model, and compensation is used to improve power transfer. After optimization, the experiment results show that the maximum power received by load is 14.4 W and maximum efficiency is 67%. The solution proposed in this paper can be easily used to existing mooring buoys to mitigate the periodical replacement of the sensor's batteries. This paper might also be seen as a reference to other similar ICPT system so as to speed up the design process.

2. System Structure

Figure 1 shows the structure of the system. The system is primarily composed of a solar panel, a buoy body, a controller, an upper coupler, a mooring cable, a lower coupler, an underwater sensor, and so on. Electric energy, which is generated by solar panels, is stored in a lead-acid battery as a power source for the whole system. Specifications of the lead-acid battery are as follows: 12 V, 150 Ah. A DC-DC converter is utilized to raise output voltage to 24 V. The principle of this ICPT system can be simplified as Figure 2 shows. The mooring cable which is the transmission media of the electric power is both the upper coupler's secondary winding and the lower coupler's primary winding. The rectangular signal can be transferred from the buoy to the underwater sensor by coupling the effects of the upper and lower couplers. The numbers of the upper coupler's secondary winding and of the lower coupler's primary winding are both one in the system.
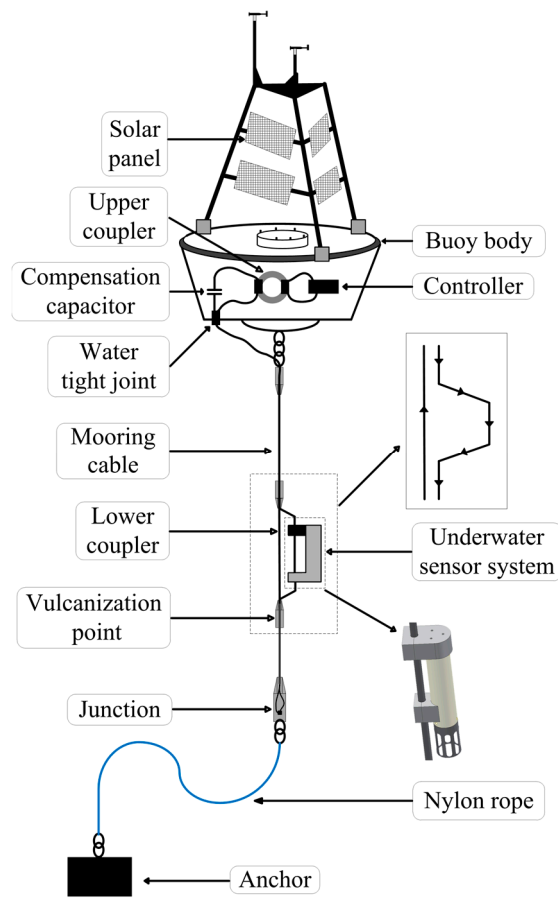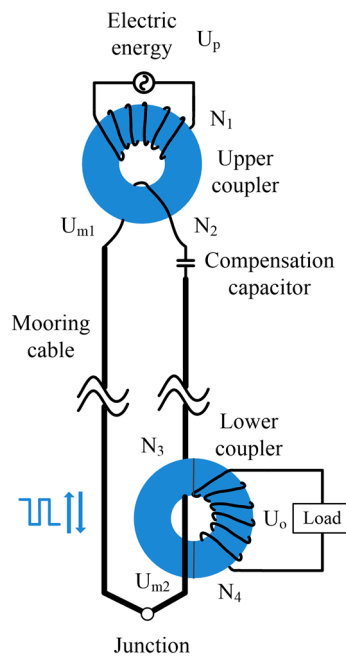
Figure 1. System structure.

Figure 2. System principle.

Under ideal conditions, the primary and secondary windings are fully coupled and all impedance is ignored, and the magnetic flux in any section of a core is identical. Therefore, equations can be obtained as follows:

$$\begin{cases} d\Phi_{11}/dt = d\Phi_{12}/dt \\ d\Phi_{21}/dt = d\Phi_{22}/dt \end{cases} \tag{1}$$

where Φ_{11} and Φ_{12}, respectively, are the magnetic flux of the upper coupler's primary and secondary windings; Φ_{21} and Φ_{22}, respectively, are the magnetic flux of the lower coupler's primary and secondary windings. According to the law of electromagnetic induction, the induced voltage can be obtained as follows:

$$\begin{cases} U_p = N_1(d\Phi_{11}/dt) \\ U_{m1} = N_2(d\Phi_{12}/dt) \\ U_{m2} = N_3(d\Phi_{21}/dt) \\ U_o = N_4(d\Phi_{22}/dt) \end{cases} \tag{2}$$

where U_p is the voltage amplitude of the rectangular signal, U_{m1} is the induced voltage of the upper coupler's secondary winding, U_{m2} is the voltage of the lower coupler's primary winding, U_o is the induced voltage of the lower coupler's secondary winding. N_1, N_2, N_3, and N_4, respectively, are the numbers of windings as shown in Figure 2. Since the mooring cable's impedance is ignored, U_{m2}, which is transferred from U_{m1}, equals U_{m1}. As a result, from Equations (1) and (2), the voltage gain of the system is

$$\frac{U_o}{U_p} = \frac{N_4}{N_3} \cdot \frac{N_2}{N_1}. \tag{3}$$

In this system, N_2 and N_3 are both one, so the ratio of U_o and U_p is N_4/N_1.

In order to invert DC power to the rectangular signal, a full-bridge inverter circuit as shown in Figure 3 is placed in the controller. The rectangular signal is achieved by the alternate switching of two groups of metal-oxide semiconductor field-effect transistors (MOSFET) at the diagonal position. Chip IR2110 (Infineon, Munich, Germany) is used to drive MOSFET at the switching frequency of pulse width modulation (PWM) waves which are generated by the ARM core chip STM32F407 (STMicroelectronics, Geneva, Switzerland). The expected voltage amplitude of the rectangular signal depends on the DC power's voltage U_d, while the frequency of the rectangular signal hinges on the PWM waves' frequency.
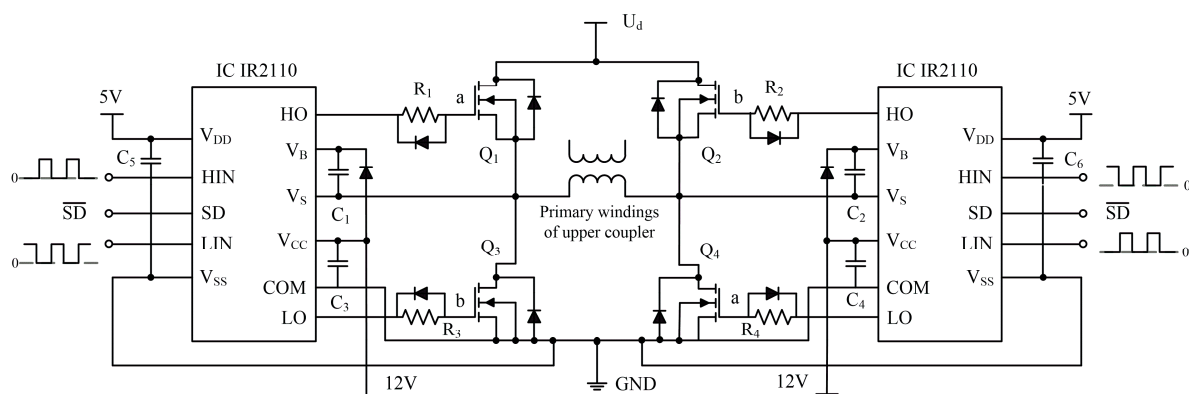

Figure 3. Full-bridge inverter circuit.

A special mooring cable is designed as shown in Figure 4. The external form of the mooring cable whose interior construction is in the form of a loop appears as a single cable by connecting two groups of interior wires at the end. The length of the mooring cable should be a little longer than the distance from the surface to the sensor's deepest mounting position in seawater. A nylon rope is used to link the mooring cable and anchor. At the underwater sensor's mounting position, the mooring cable is

separated into two parts to leave space for the installation of the coupler. At the top, the mooring cable is connected to the buoy by a connector, and the cable's two groups of wires are connected as the upper coupler's secondary coil in the buoy body.
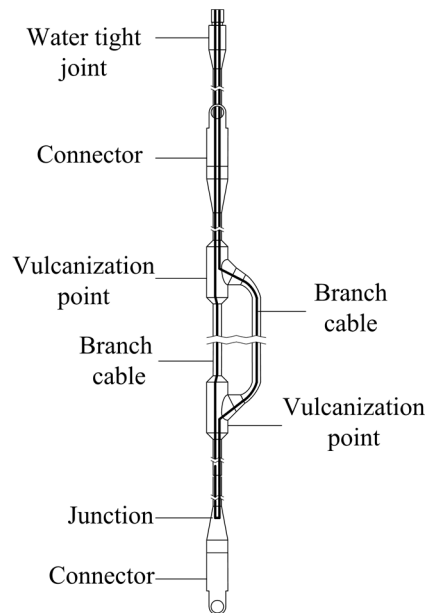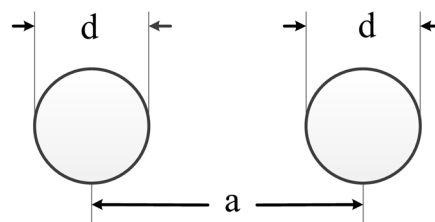

Figure 4. Structure of the mooring cable.

As Figure 4 shows, the length of the branch cable is so small that the cable can be equivalent to a set of parallel wires as shown in Figure 5. According to [20], the inductance of cable can be calculated as follows:

$$L = 4l \left(\ln \frac{2a}{d} - \frac{a}{l} \right) \times 10^{-7} (\text{H}) \tag{4}$$

where *l* is the length of the parallel wires, *d* is the diameter of wire, and *a* is the distance between the two parallel wires. All of the above units are in m. According to Figure 4, the values of parameters *l*, *d*, and *a* are fixed; therefore, the inductance of the mooring cable can be considered changeless.

Figure 5. Parallel wires.

In order to verify the theoretical analysis, the simulations of the mooring cable's inductance are carried out by Ansoft Maxwell. There is a shielding layer outside the wires to reduce the influence of the seawater. The parameters of the mooring cable applied in the simulation and following analysis are as follows: the length is 12 m, the distance between the two groups of wires is 3 cm, and the diameter of each group of wires is 4 mm. The simulation is carried out as shown in Figure 6. Results show that the mooring cable's inductance in air and seawater, respectively, is 13.8 and 13.9 µH. It can be observed that the inductance in the air and seawater is very close. Most importantly, we rented a ship to put the mooring cable in the seawater and measure the inductance of the mooring cable in the condition of

bending, and the result indicates that the variation range of inductance is smaller than 0.1 µH, and the value is very close to that in air.
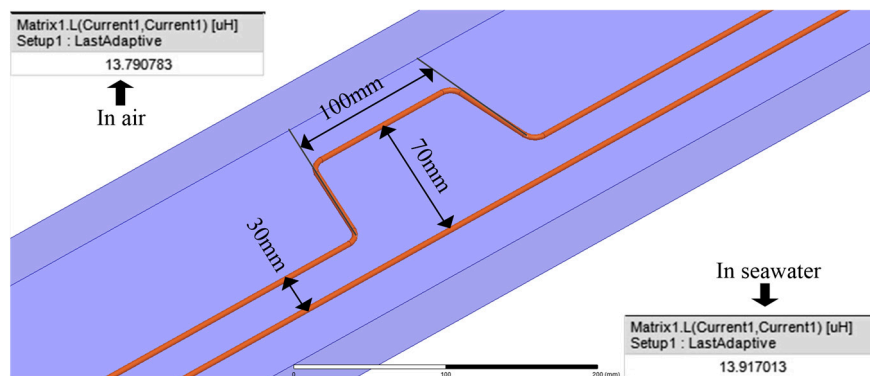

Figure 6. Simulations of the mooring cable's inductance.

Compared with the traditional ICPT system, there are two couplers and a ring-form cable in this system. This will make the system model distinctive from the traditional ICPT system and have its own particularity.

3. Theoretical Modeling

The mutual inductance model and the T type model are commonly applied to analyze the coupling effect in ICPT systems [21–23]. The mutual inductance model that utilizes the induced voltage to describe the coupling effect is considered simpler than the T type mode in the analysis procedure. Thus, the system mutual inductance model is established and shown in Figure 7.
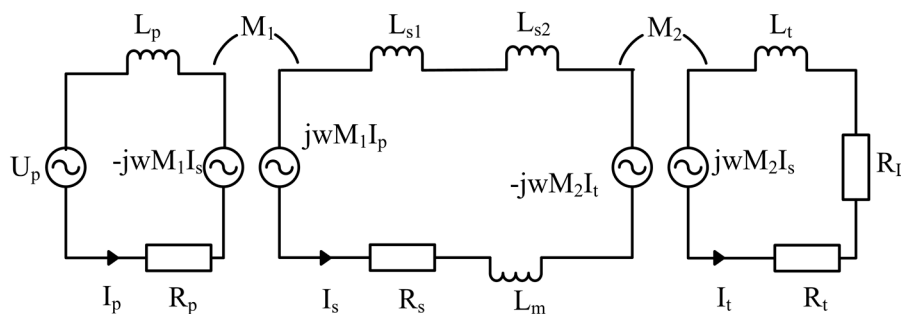

Figure 7. System model.

The model's associated parameters are summarized in Table 1. It is critical that the mooring cable's inductance is separated equivalently. According to the mutual inductance models, L_{s1} and L_{s2}, respectively, are the self-inductance of the upper coupler's secondary and the lower coupler's primary windings. L_{s1} equals the self-inductance related to the part of the mooring cable that threads through the upper magnetic core, L_{s2} equals the self-inductance related to the part of the mooring cable that threads through the lower magnetic core. The numbers of the upper coupler's secondary winding and the lower coupler's primary winding are both one. The windings' length that threads through the magnetic cores is so small that the decrease of the mooring cable's inductance brought by separation can be ignored. Therefore, L_m in Table 1 approximately equals the inductance of the mooring cable with no magnetic cores mounted. Through the above separation, it can be observed that L_{s1} and L_{s2} do not vary with the mooring cable's length, and L_m is constant due to the analysis in Section 2.

Table 1. Configuration parameters.

Factors	Symbol
Mutual inductance of upper coupler's primary winding and mooring cable	M_1
Mutual inductance of mooring cable and lower coupler's secondary winding	M_2
Amplitude of rectangular signal	U_p
Resistance of upper coupler's primary winding	R_p
Self-inductance of upper coupler's primary winding	L_p
Resistance of mooring cable	R_s
Self-inductance of upper coupler's secondary winding	L_{s1}
Self-inductance of lower coupler's primary winding	L_{s2}
Inductance of mooring cable	L_m
Resistance of lower coupler's secondary winding	R_t
Self-inductance of lower coupler's secondary winding	L_t
Load's equivalent resistance	R_L
Angular frequency of rectangular signal	ω

We introduce a new parameter L_s to facilitate analysis. It is defined as follows:

$$L_s = L_{s1} + L_{s2} + L_m. \tag{5}$$

Then, the mathematical expressions of the system's three current loops can be obtained as follows:

$$\begin{cases} U_p = I_p R_p + j\omega I_p L_p - j\omega M_1 I_s \\ j\omega M_1 I_p = I_s R_s + j\omega I_s L_s - j\omega M_2 I_t \\ j\omega M_2 I_s = I_t R_t + j\omega I_t L_t + I_t R_L \end{cases} \tag{6}$$

where U_p is the voltage amplitude of the rectangular signal, and ω is the angular frequency of the rectangular signal. I_p, I_s, and I_t, respectively, are current in the upper coupler's primary winding, the mooring cable, and the lower coupler's secondary winding. Let

$$\begin{cases} Z_1 = j\omega L_p + R_p \\ Z_2 = j\omega L_s + R_s \\ Z_3 = j\omega L_t + R_t \end{cases} . \tag{7}$$

The equations of the three loops' current can be obtained from Equations (6) and (7):

$$I_p = \frac{U_p \left[Z_2(Z_3 + R_L) + \omega^2 M_2^2 \right]}{\left[Z_1 Z_2(Z_3 + R_L) + Z_1 \omega^2 M_2^2 \right] + \omega^2 M_1^2(Z_3 + R_L)} \tag{8}$$

$$I_s = \frac{U_p [j\omega M_1(Z_3 + R_L)]}{\left[Z_1 Z_2(Z_3 + R_L) + Z_1 \omega^2 M_2^2 \right] + \omega^2 M_1^2(Z_3 + R_L)} \tag{9}$$

$$I_t = \frac{-U_p \omega^2 M_1 M_2}{\left[Z_1 Z_2(Z_3 + R_L) + Z_1 \omega^2 M_2^2 \right] + \omega^2 M_1^2(Z_3 + R_L)} . \tag{10}$$

The coefficient of mutual inductance, which changes with the windings' number, the position, the dimension, and so on, will bring difficulties to the analysis of the model. From [24], the coupling factor k primarily associated with the section of the magnetic core is relatively stable. The expression of k is defined in (11) [25].

$$\begin{cases} k = \sqrt{k_a k_b} = M/\sqrt{L_a L_b} \\ k_a = \frac{\Phi_{ba}}{\Phi_a} \\ k_b = \frac{\Phi_{ab}}{\Phi_b} \end{cases} \tag{11}$$

where L_a and L_b, respectively, are the self-inductance of the coupler's primary winding (Coil A) and the secondary winding (Coil B), Φ_a is the total flux of the primary winding when it is excited, and Φ_b is the total flux of the secondary winding when it is excited. Φ_{ba} and Φ_{ab}, respectively, are the fractions of Φ_a and Φ_b that link the corresponding coil, and k_b and k_b, respectively, are the coupling factors when Coil A or Coil B acts as the primary coil. In this paper, k_1 and k_2 which, respectively, are the upper and lower coupler's coupling factors, can be obtained by replacing L_a and L_b in (11) with L_p, L_{s1} or L_{s2}, L_t in Table 1. For a certain ICPT system similar to this paper, the coupling factor is constant.

Therefore, in order to facilitate the analysis, we use the coupling factor to replace the coefficient of mutual inductance. The voltage of the load can be described by the following equation:

$$U_L = \frac{-U_p \omega^2 k_1 k_2 \sqrt{L_p L_{s1} L_{s2} L_t} R_L}{\left[Z_1 Z_2 (Z_3 + R_L) + Z_1 \omega^2 k_2^2 L_{s2} L_t \right] + \omega^2 k_1^2 L_p L_{s1} (Z_3 + R_L)} \tag{12}$$

where k_1 and k_2, respectively, are the coupling factors of the upper and lower couplers. The voltage gain A_U, power P_L, and efficiency η can be obtained as follows:

$$A_U = \left| \frac{-\omega^2 k_1 k_2 \sqrt{L_p L_{s1} L_{s2} L_t} R_L}{\left[Z_1 Z_2 (Z_3 + R_L) + Z_1 \omega^2 k_2^2 L_{s2} L_t \right] + \omega^2 k_1^2 L_p L_{s1} (Z_3 + R_L)} \right| \tag{13}$$

$$P_L = \left| \frac{U_p^2 \omega^4 k_1^2 k_2^2 L_p L_{s1} L_{s2} L_t R_L}{\left\{ \left[Z_1 Z_2 (Z_3 + R_L) + Z_1 \omega^2 k_2^2 L_{s2} L_t \right] + \omega^2 k_1^2 L_p L_{s1} (Z_3 + R_L) \right\}^2} \right| \tag{14}$$

$$\eta = \left| \frac{\omega^4 k_1^2 k_2^2 L_p L_t L_{s1} L_{s2} R_L}{\left\{ \left[Z_1 Z_2 (Z_3 + R_L) + Z_1 \omega^2 k_2^2 L_{s2} L_t \right] + \omega^2 k_1^2 L_p L_{s1} (Z_3 + R_L) \right\} \left(\omega^2 k_2^2 L_{s2} L_t + Z_2 R_L + Z_2 Z_3 \right)} \right| \tag{15}$$

It can be observed that the voltage gain A_U, power P_L, and efficiency η, which are summarized as the power transfer performance, are related to the coupling factor, the frequency, the inductance of windings, and the impedance of the mooring cable.

4. Parameter Analysis and Compensation

A prototype system is established with original parameters as shown in Table 2. Upper and lower magnetic cores are all the same in material and size. The material of the magnetic core is Mn–Zn ferrite with a relative initial permeability of 10^4. The shape is annular, and the size is 85.7 mm (outer diameter) × 55.5 mm (inner diameter) × 25.4 mm (thickness). The magnetic core is separated into two halves with an air-gap to facilitate the installation. The end faces of the core are mirror-finished, and the air-gap can be estimated to be smaller than 1 μm. Copper-made Litz wires are used as the winding wires with parameters as follows: 0.2 mm (single wire diameter) × 20 (number of threads). The original number of the upper coupler's primary and that of the lower coupler's secondary windings are both 7. To the ferrite core, under the low power and frequency condition in this paper, the core loss is so small that it is ignored in the analysis. The parameter analysis is carried out based on the system model.

Table 2. Prototype's original parameters.

Parameters	Values
U_p	24 (V)
R_P	85 (mΩ)
L_P	781.4 (μH)
R_s	36.8 (mΩ)
L_{s1}	18.42 (μH)
L_{s2}	18.58 (μH)
L_m	14.8 (μH)
R_t	134.2 (mΩ)
L_t	877.5 (μH)
R_L	50 (Ω)
ω	2.51×10^5 (rad/s)

4.1. Analysis of Coupling Factor

The coupling factor, which is a very important parameter in the ICPT system, can affect the power transfer performance [26]. Expressions of voltage gain A_U, power P_L, and efficiency η are shown as Equations (13)–(15) in Section 3. By substituting parameter values in Table 2 to Equations (13)–(15), the equations covered the power transfer performance, and k_1 and k_2 could be obtained. According to the equations, the surface diagrams of the relationship between the power transfer performance and k_1 and k_2 can be obtained as shown in Figure 8.
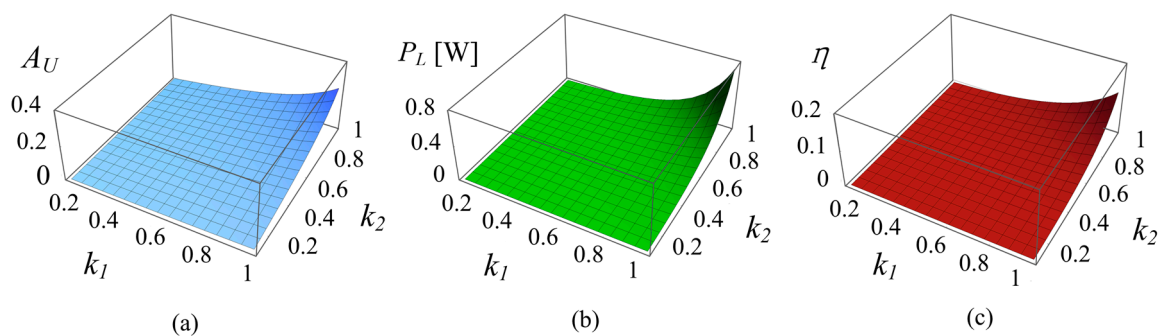
Figure 8. (**a**) Surface diagram of voltage gain related to coupling factor; (**b**) Surface diagram of power related to coupling factor; (**c**) Surface diagram of efficiency to coupling factor. (A_U: voltage gain; P_L: power; η: efficiency; k_1: coupling factor of upper coupler; k_2: coupling factor of lower coupler).

The result shows that all three indicators of power transfer performance increase with k_1 and k_2. From the definition of the coupling factor in (11), a higher coupling factor will lead to a larger mutual flux at the same total flux and then a higher induced voltage can be obtained in the secondary winding.

The coupling factor is primarily related to the structure of the core, especially the air-gap between the two half cores. The large air-gap will lead to an extremely low coupling factor. Couplers in this system are composed of two semicircular halves to make the installation expedient. A sealing device is produced to isolate the seawater and impact the two half magnetic cores closely. The practical measured values of coupling factors are $k_1 = k_2 = 0.96$. These values are used in the following analysis. In this paper, Multisim is used to simulate the power transfer in order to verify the model. The details of the simulation model are shown in Figure 9. The load's voltage waveforms with different coupling factors obtained by simulation are shown in Figure 10. Results coincide with mathematical analysis.
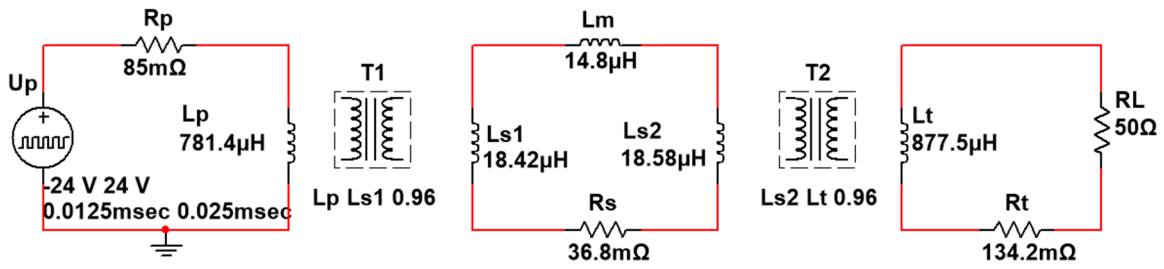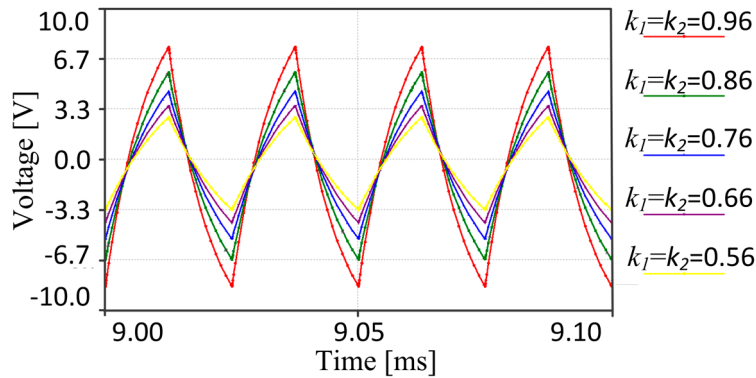
Figure 9. Simulation by Multisim.

Figure 10. Simulation of voltage waveforms of the load (comparison of the coupling factors).

4.2. Analysis of Frequency

There is a typical working frequency range to a specific magnetic core. According to the principle of the transformer, equations can be obtained as follows:

$$
\begin{cases}
e = -N\dfrac{d\Phi}{dt} \\
\Phi = BA = \dfrac{Li}{N}
\end{cases}
\tag{16}
$$

where e is the induced voltage, Φ is the magnetic flux, B is the magnetic flux density, N is the turn of winding, and A is the area of the core section. The signal's cycle length is inversely proportional to the frequency. When fixing the induced voltage, according to Equation (16), the magnetic flux imported to the coupler will be small, while the frequency becomes excessively high. Then, i will be small since L and N are fixed. The voltage source is used as the power source in this system; therefore, the power transfer will be small as the current becomes small. The frequency cannot be excessively small, because this will lead to a high current and power loss in the mooring cable and windings. A suitable frequency is important to this system.

The parameter values in Table 2 are substituted to Equations (13)–(15), and the influence of frequency of the power transfer performance is analyzed. Curve charts of power transfer performance related to the frequency are shown in Figure 11.
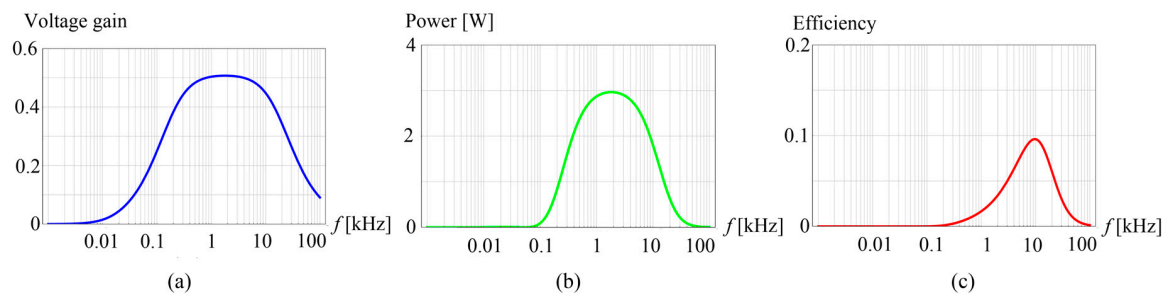
Figure 11. (**a**) Curve chart of voltage gain related to frequency; (**b**) Curve chart of power related to frequency; (**c**) Curve chart of efficiency related to frequency. (*f*: frequency).

From Figure 11, it can be seen that frequency values that make power transfer and efficiency reach their maximums are not identical. When the frequency equals 1.8 kHz, the voltage gain and the power achieve maximums simultaneously, and the maximum power is 3 W. When frequency equals 9.7 kHz, the efficiency achieves a maximum and the value is 9.6%. The simulation results of the maximum power transferred and efficiency are as follows:

$$1.8 \, \text{kHz}: \ P_L = 2.8 \text{W}, \eta = 3.2\%$$

$$9.7 \, \text{kHz}: \ P_L = 2 \text{W}, \eta = 9.2\%.$$

As the model calculations are ideal, results of the simulation are somewhat different.

4.3. Analysis of Coupler's Winding

In this system, turns of the upper coupler's secondary and the lower coupler's primary winding are both fixed at a value of one. Thus, only the influence of the upper coupler's primary and the lower coupler's secondary windings is discussed. The influence of the coupler's windings behaves chiefly as an impact of the windings' self-inductance. Since the material and the structure of the upper and lower couplers are all the same, to simplify the analysis, let $L_p = L_t = L$. Thus, turns of the upper coupler's primary winding and the lower coupler's secondary winding are equal. According to Equation (16), changes of inductance will affect the current. When L (excited inductance) becomes small, the current and the loss in the windings and the mooring cable become large. On the other hand, when L becomes large, the current received by the load becomes small. Thus, it is necessary to take account of loss and power when assigning values to L.

Substituting parameter values in Table 2 to Equations (13)–(15), the curve charts of the power transfer performance related to the coupler's windings can be obtained, as Figure 12 shows.
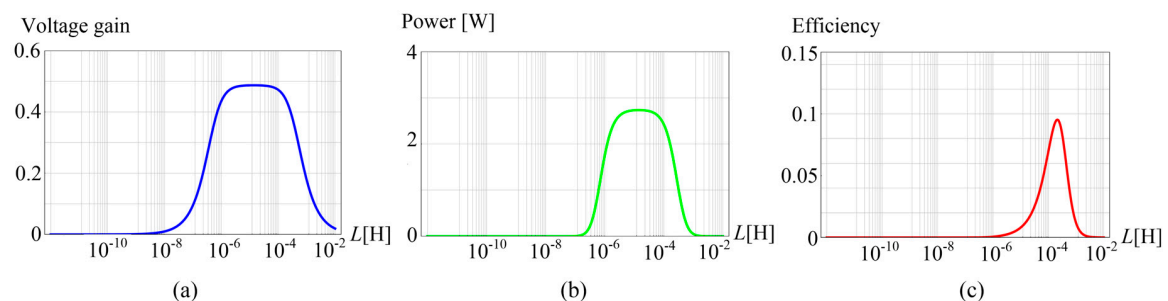
Figure 12. (**a**) Curve chart of voltage gain related to coupler's windings; (**b**) Curve chart of power related to coupler's windings; (**c**) Curve chart of efficiency related to coupler's windings. (*L*: self-inductance of windings).

As shown in Figure 12, the power of the load reaches maximum 2.7 W when $L = 14.3$ μH (turn is about 1); however, the current at that time is very high. Efficiency reaches a maximum value of 9.5% when $L = 211$ μH (turn is about 2). The simulation results of the maximum power and efficiency are as follows:

$$L = 14.3 \text{ μH}: \ P_L = 2.7 \text{ W}, \ \eta = 1.2\%$$

$$L = 211 \text{ μH}: \ P_L = 1.8 \text{ W}, \ \eta = 9.4\%.$$

Through analyzing the current in the system, we found that the influence of the coupler's windings presents as the effect of the current in the system. When power reaches a maximum, losses in windings and the mooring cable are significant, such that efficiency is very low at that time.

4.4. Analysis of Mooring Cable and Compensation

According to the system model, the impedance of the mooring cable is represented by L_{s1}, L_{s2}, L_m, and R_s. The relationship between L_{s1}, L_{s2}, L_m, and L_s are defined in Equation (5). Similarly, surface diagrams of the power transfer performance related to L_s and R_s are obtained as shown in Figure 13.
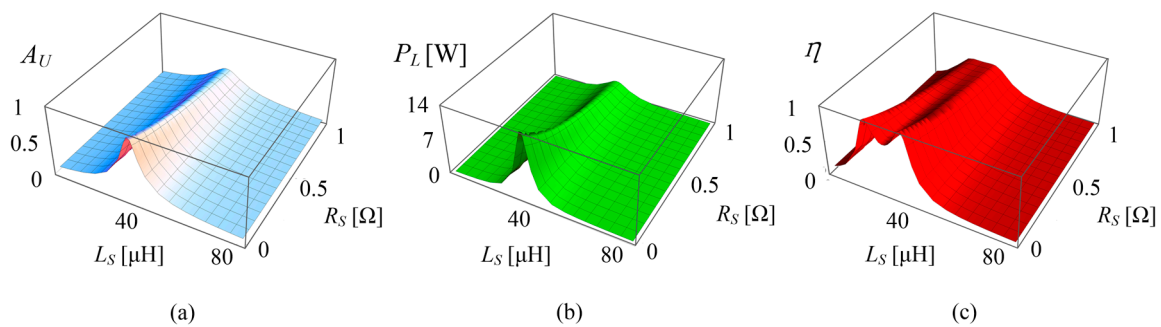
Figure 13. (**a**) Surface diagram of voltage gain related to mooring cable's impedance; (**b**) Surface diagram of power related to mooring cable's impedance; (**c**) Surface diagram of efficiency to mooring cable's impedance. (A_U: voltage gain; P_L: power; η: efficiency; L_S: inductance of the mooring cable; R_S: resistance of the mooring cable).

From Figure 13, it can be observed that the smaller R_s is, the higher the power transfer performance will be. Since there is an alternating current in the mooring cable, Litz wires are utilized to reduce the influence of the skin effect. Lower resistivity is also necessary to the mooring cable. There is one value of L_s that makes A_U and P_L reach their maximums, whereas there are two values of L_s that make η reach its maximum.

Substituting parameter values except for L_s in Table 2 to Equations (13)–(15), values of L_s that make power and efficiency reach their maximums can be obtained by solving the equations. Results show that, when L_s equals 33.97 μH, A_U and P_L reach their maximums, and maximum power is 12.9 W; when L_s equals 17.2 μH or 33.21 μH, only η can reach its maximum, and maximum efficiency is 85.2%. However, when L_s equals 17.2 μH, the voltage gain and power are very small. Consequently, the value of L_s that makes power and efficiency reach their maximums are almost the same, and L_{sMAX} is used to represent it.

The summation of the self-inductance of the upper coupler's secondary winding and the lower coupler's primary winding is

$$L_{s1} + L_{s2} = L_s - L_m = 37 \text{ μH}. \tag{17}$$

Comparing the value with L_{sMAX}, we find

$$L_{sMAX} = L_{s1} + L_{s2} \tag{18}$$

According to the analysis above and Equation (18), the smaller the self-inductance of the mooring cable is, the higher the power transfer performance will be. This is because reactive power, which is generated by the inductance element, has a strong impact on power transfer. LC resonant compensation can be used to reduce the influence of the inductance element in the ICPT system. To implement compensation, the compensation capacitor is added to the mooring cable as shown in Figures 1 and 2. The principle of compensation is that the imaginary part of the system's whole impedance equals zero. According to the system model and the parameters in Table 2, the value of the compensation capacitor is calculated to be 0.86 μF. Surface diagrams of power transfer performance related to the compensation capacitor are obtained as shown in Figure 14. It can be observed that, when the compensation capacitor equals 0.86 μF, the power transfer and efficiency reach maximums.
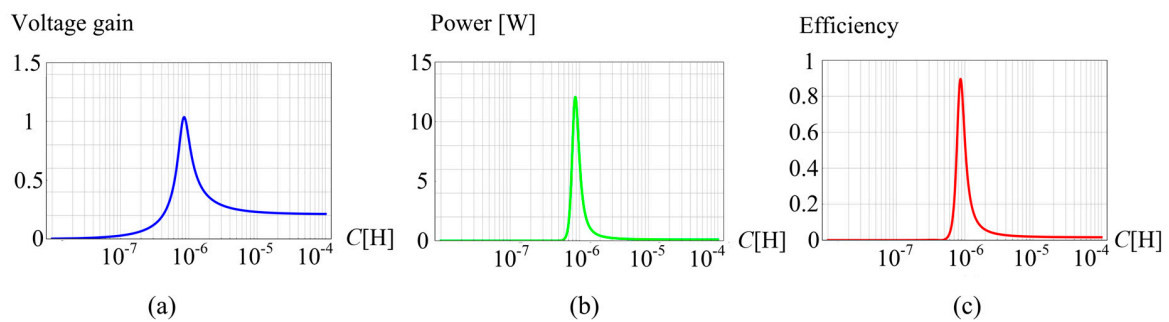
**Figure 14.** (**a**) Curve chart of voltage gain related to compensation capacitor; (**b**) Curve chart of power related to compensation capacitor; (**c**) Curve chart of efficiency to compensation capacitor. (*C*: compensation capacitor).

From the analysis in Sections 4.1–4.4, it can be found that, although adjusting the coupling factor, the frequency, and the coupler's winding can improve the system's power transfer, the effect is not significant. Applying resonant compensation is able to gain a higher power transfer and efficiency.

5. Optimization and Experiments

Experiments were carried out to verify the accuracy of model. Experimental setup is shown in Figure 15. A DC power supply was used as the power source. Parameters of the couplers are introduced in the above section. The mooring cable was specially made with a looped internal structure. High power resistance was used as the load. A wattmeter was used to measure the power received by the load, and the current probe and the oscilloscope were used to observe the waveform of the current in the mooring cable and the voltage waveform of the load.
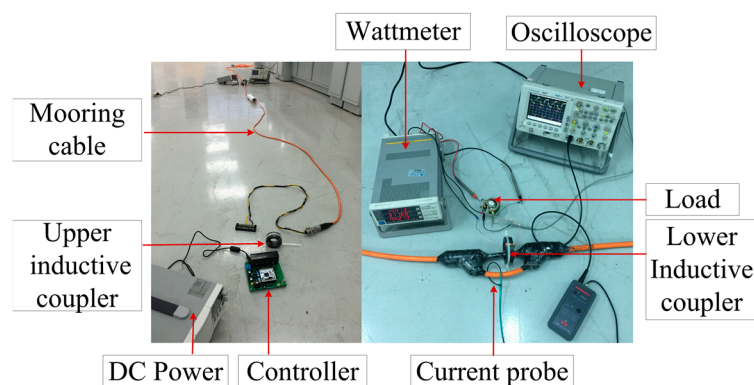
Figure 15. Experimental setup.

5.1. Experiment of Original Prototype

The parameters in Table 2 are the original parameters as the experimental platform was established. The power transfer experiment with original parameters was carried out. Waveforms of the load's voltage and current in the mooring cable were obtained by oscilloscope as shown in Figure 16. The power received by the load and efficiency are summarized in Table 3. The results can be used as a reference to the optimized results.
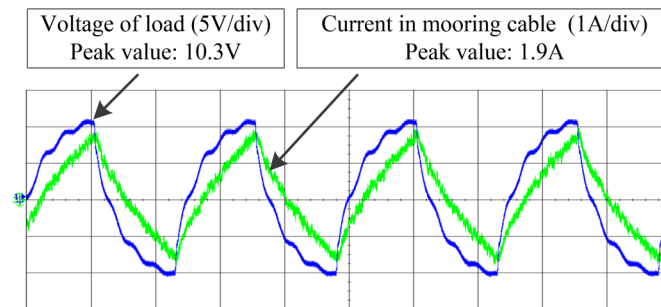


Figure 16. Experiment of original parameters.

Table 3. Experiment results.

Parameters	Original	Max P_L	Max η
Frequency of rectangular signal	40 (kHz)	40 (kHz)	40 (kHz)
Inductance of upper coupler's primary winding L_p	781.4 (μH) (7 turns)	64.2 (μH) (2 turns)	781.4 (μH) (7 turns)
Inductance of lower coupler's secondary winding L_t	877.5 (μH) (7 turns)	72.8 (μH) (2 turns)	877.5 (μH) (7 turns)
Load's resistance	50 (Ω)	50 (Ω)	50 (Ω)
Compensation capacitance	None	0.45 (μF)	0.81 (μF)
Power load	1 (W)	14.4 (W)	6.3 (W)
Efficiency	27.7%	26.3%	67%
Amplitude of load's voltage	10.3 (V)	45.6 (V)	26.7 (V)
Amplitude of mooring cable's current	2.23 (A)	5.7 (A)	4.7 (A)

*5.2. Optimization of Parameters and Experiments*

According to the model analysis, compensation can significantly improve the power transfer and efficiency. Meanwhile, the frequency of the rectangular signal and the coupler's winding can also affect the power transfer performance. To find out the maximum power received by the load and efficiency, two series of experiments were carried out. All experiments were implemented under compensation. The difference is that one series of experiments was implemented with different frequencies, and the other series of experiments was implemented with a different coupler's windings.

The parameters of the experiments with different frequencies are identical to that in Table 2. Since no capacitor can make a system resonant below 20 kHz, experiments were carried out from 20 kHz. The experiment results of the power load and efficiency are shown in Figure 17. It can be observed that the system achieves a maximum power transfer of 7 W at 20 kHz, and efficiency reaches a maximum value of 67% at 40 kHz.
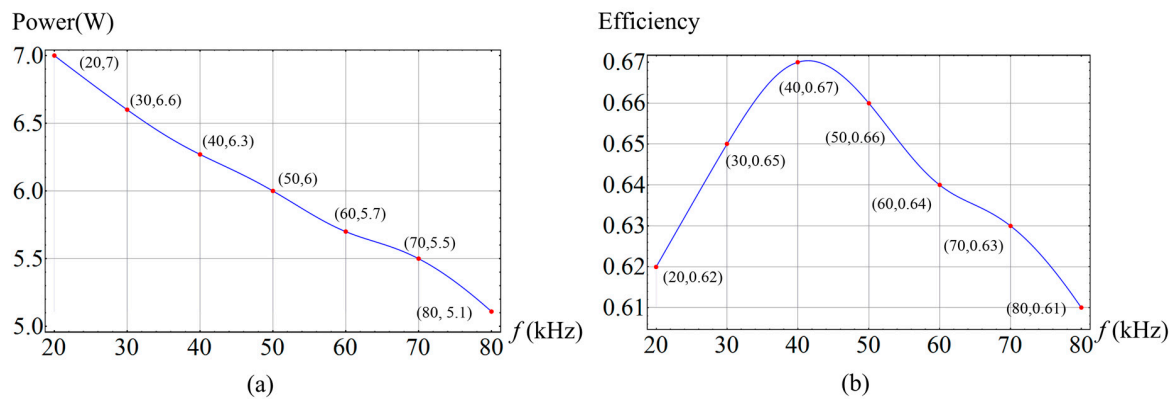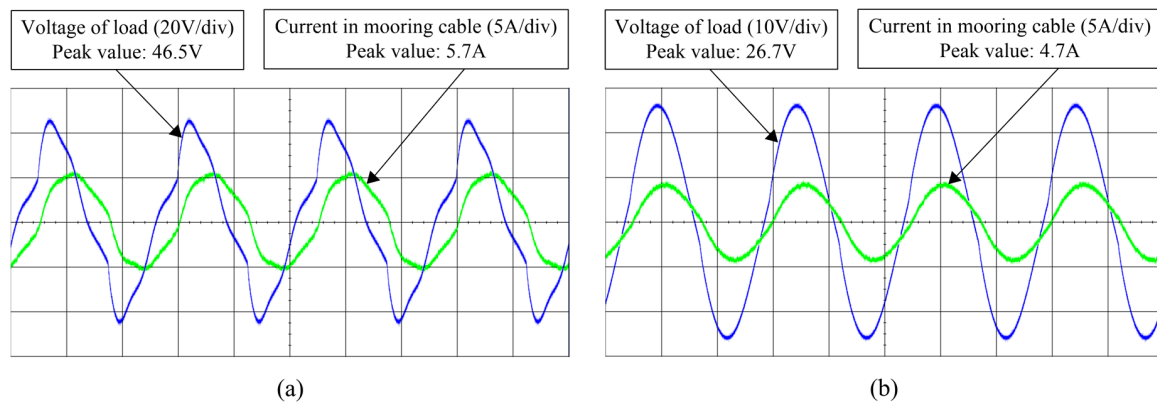
Power(W)

Efficiency

Figure 17. (**a**) Experiment results of power load related to frequency; (**b**) Experiment results of efficiency related to frequency.

The parameters of the experiments with a different coupler's windings are identical to that in Table 2. In the experiment, turns of the upper coupler's primary winding and the lower coupler's secondary winding are uniform. From the analysis in Section 4.3, the current will be very large when the turn is small. Since the limit of the power source's maximum output current, the changes of the turns are in the range of 2–8. The experimental results of the power load and the efficiency are shown in Figure 18. It can be observed that the system achieves a maximum power transfer of 14.4 W in two turns, and efficiency reaches a maximum value of 67% in seven turns.
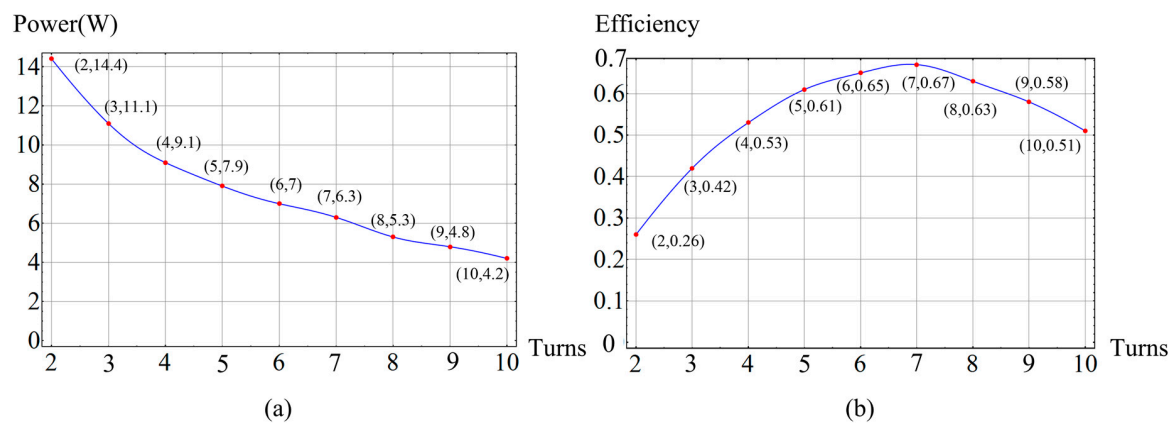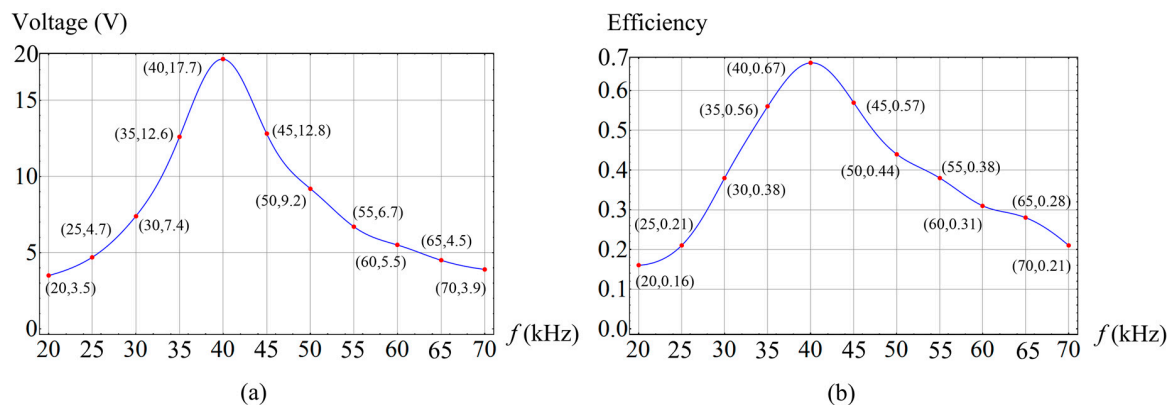
Power(W)

Efficiency

Figure 18. (**a**) Experiment results of power load related to windings; (**b**) Experiment results of efficiency related to windings.

From the above experiments, we found that the maximum power received by the load is 14.4 W and that the maximum efficiency of the system is 67%. Waveforms of load voltage and current in mooring cable are shown as Figure 19. The experiment results and system's crucial parameters are summarized in Table 3. When the load receives maximum power, the current in the mooring cable is high, and this will lead to large losses. Therefore, the efficiency is relatively low at that time.

Figure 19. (**a**) Waveforms in the condition of a maximum power load; (**b**) Waveforms in the condition of maximum efficiency.

To verify that the system achieves a maximum power transfer performance in resonant frequency, a series of experiments was carried with frequencies out of the resonant frequency. A point of maximum efficiency was selected to implement the experiment. A wattmeter was used to measure the effective value of the load's voltage and efficiency. Graphs of the load's voltages and efficiencies related to different frequencies (20 to 70 kHz) were obtained as shown in Figure 20. It can be observed from the results that the load's voltages and efficiencies quickly decrease when the operating frequency leaves the resonant frequency.

Figure 20. (**a**) Experiment results of load voltage related to frequencies; (**b**) Experiment results of efficiency related to frequencies.

This system's power transfer performance can be improved by adjusting the frequency and windings, and by applying compensation. To a system with certain parameters, maximum power and efficiency can be obtained at resonant frequency. Compared with the experiment of the original parameters, the result of the optimized experiment improves considerably in the load's voltage and current in the mooring cable, which leads to a great promotion in maximum power transfer and efficiency.

6. Conclusions

This paper proposes a new ICPT system for underwater sensors of ocean buoys. The system can be expected to allow real-time power supplying and easier attachment for underwater sensors. A special mooring cable is designed to make this system have a high value of practical application. The theoretical model for this particular system is established in this paper, which allows for data

transmission by the same principle of another coil in the upper coupler. Various simulations and experiments were carried out to verify the model and improve the power transfer. This ICPT system and analytical methods can help solve the problem of power supply to the underwater sensors of buoys and accelerate the design progress of similar systems.

Author Contributions: Cheng Fang designed the structure, built the model, did the analysis and wrote the paper. Xingfei Li as research supervisor provided guidance as well as funding for the research and key suggestions for writing this paper. Ziming Xie carried out the simulation. Jiayi Xu and Linling Xiao designed the full bridge converter and did the experiment.

Conflicts of Interest: The authors declare no conflict of interest.

References

1. Reza, M.M.; Rahman, K.T.; Zakaria, A.S.M.; Reza, M.M. Grid based fuzzy optimized routing protocol for underwater sensor networks. *Int. J. Comput. Appl.* **2015**, *112*, 23–26.
2. Jha, D.K.; Wettergren, T.A.; Ray, A.; Mukherjee, K. Topology optimisation for energy management in underwater sensor networks. *Int. J. Control* **2015**, *88*, 1–14. [CrossRef]
3. Rault, T.; Bouabdallah, A.; Challal, Y. Energy efficiency in wireless sensor networks: A top-down survey. *Comput. Netw.* **2014**, *67*, 104–122. [CrossRef]
4. Mcdonough, M. Integration of Inductively Coupled Power Transfer and Hybrid Energy Storage System: A Multi-Port Power Electronics Interface for Battery Powered Electric Vehicles. *IEEE Trans. Power Electron.* **2015**, *30*, 6423–6433. [CrossRef]
5. Raju, S.; Wu, R.; Chan, M.; Yue, C.P. Modeling of Mutual Coupling between Planar Inductors in Wireless Power Applications. *IEEE Trans. Power Electron.* **2014**, *29*, 481–490. [CrossRef]
6. Misawa, T.; Takura, T.; Sato, F.; Sato, T. Parameter Design for High-Efficiency Contactless Power Transmission under Low-Impedance Load. *IEEE Trans. Magn.* **2013**, *49*, 4164–4167. [CrossRef]
7. Tsai, M.C.; Chiou, K.Y.; Wang, S.H.; Lin, C.K. Characteristics Measurement of Electric Motors by Contactless Eddy-Current Magnetic Coupler. *IEEE Trans. Magn.* **2014**, *50*, 8203804. [CrossRef]
8. Jiang, H.; Zhang, J.; Lan, D.; Liou, S.; Shahnasser, H.; Fechter, R.; Hirose, S.; Harrison, M.; Roy, S. A low-frequency versatile wireless power transfer technology for biomedical implants. *IEEE Trans. Biomed. Circ. Syst.* **2013**, *7*, 526–535. [CrossRef] [PubMed]
9. Smeets, J.P.C.; Overboom, T.T.; Jansen, J.W.; Lomonova, E.A. Comparison of Position-Independent Contactless Energy Transfer Systems. *IEEE Trans. Power Electron.* **2013**, *28*, 2059–2067. [CrossRef]
10. Cheng, Z.; Lei, Y.; Song, K.; Zhu, C. Design and Loss Analysis of Loosely Coupled Transformer for an Underwater High-power Inductive Power Transfer System. *IEEE Trans. Magn.* **2014**, *51*, 8401110.
11. Fukuda, H.; Kobayashi, N.; Shizuno, K.; Yoshida, S.; Tanomura, M.; Hama, Y. New concept of an electromagnetic usage for contactless communication and power transmission in the ocean. In Proceedings of the IEEE Underwater Technology Symposium, Tokyo, Japan, 5–8 March 2013.
12. Kojiya, T.; Sato, F.; Matsuki, H.; Sato, T. Automatic power supply system to underwater vehicles utilizing non-contacting technology. In Proceedings of the IEEE TECHNO-OCEAN, Kobe, Japan, 9–12 November 2004; pp. 2341–2345.
13. Kojiya, T.; Sato, F.; Matsuki, H.; Sato, T. Construction of non-contacting power feeding system to underwater vehicle utilizing Electro Magnetic Induction. In Proceedings of the Europe Oceans, Brest, France, 20–23 June 2005; pp. 709–712.
14. Assaf, T.; Stefanini, C.; Dario, P. Autonomous underwater biorobots: A wireless system for power transfer. *IEEE Robot. Autom. Mag.* **2013**, *20*, 26–32. [CrossRef]
15. Oiler, J.; Anderson, G.; Bana, V.; Phipps, A. Thermal and biofouling effects on underwater wireless power transfer. In Proceedings of the IEEE Wireless Power Transfer Conference, Boulder, CO, USA, 13–15 May 2015.
16. Heeres, B.J.; Novotny, D.W.; Divan, D.M.; Lorenz, R.D. Contactless underwater power delivery. In Proceedings of the IEEE Power Electronics Specialists Conference, Taipei, Taiwan, 20–25 June 1994; pp. 418–423.

17. Yoshioka, D.; Sakamoto, H.; Ishihara, Y.; Matsumoto, T.; Timischl, F. Power Feeding and Data-Transmission System Using Magnetic Coupling for an Ocean Observation Mooring Buoy. *IEEE Trans. Magn.* **2007**, *37*, 2663–2665. [CrossRef]

18. Li, X.F.; Li, C.; Lin, J.; Zhang, Q. Contactless power feeding for ocean buoy. In Proceedings of Sixth International Symposium on Precision Engineering Measurements and Instrumentation, Hangzhou, China, 8–11 August 2010.

19. Lin, J.; Li, X.F.; Zhang, Q.; Xiang, H.B. Construction of Contactless Power Feeding System for Ocean Buoy. In Proceedings of the 7th International Conference on Wireless Communications, Networking and Mobile Computing, Wuhan, China, 23–25 September 2011.

20. Harry, H. *Calculation of Inductance in Inductance*, 1st ed.; Yuan, L., Ed.; National Defense Industry Press: Beijing, China, 1960; pp. 7–8.

21. Kurschner, D.; Rathge, C.; Jumar, U. Design Methodology for High Efficient Inductive Power Transfer Systems with High Coil Positioning Flexibility. *IEEE Trans. Ind. Electron.* **2011**, *60*, 372–381. [CrossRef]

22. Moradewicz, A.; Kazmierkowski, M. High efficiency contactless energy transfer system with power electronic resonant converter. *Bull. Pol. Acad. Sci. Tech. Sci.* **2009**, *57*, 375–381. [CrossRef]

23. Abdolkhani, A.; Hu, A.P.; Nair, N.C.K. Modelling and Parameters Identification of Through-Hole Type Wind Turbine Contactless Sliprings. *Engineering* **2012**, *4*, 272–283. [CrossRef]

24. Elliott, G.A.J.; Covic, G.A.; Kacprzak, D.; Boys, J.T. A New Concept: Asymmetrical Pick-Ups for Inductively Coupled Power Transfer Monorail Systems. *IEEE Trans. Magn.* **2006**, *42*, 3389–3391. [CrossRef]

25. Boys, J.T.; Elliott, G.A.J.; Covic, G.A. An Appropriate Magnetic Coupling Co-Efficient for the Design and Comparison of ICPT Pickups. *IEEE Trans. Power Electron.* **2007**, *22*, 333–335. [CrossRef]

26. Li, H.L.; Hu, A.P.; Covic, G.A.; Tang, C.S. Optimal coupling condition of IPT system for achieving maximum power transfer. *Electron. Lett.* **2009**, *45*, 76–77. [CrossRef]